

INERTIA FRICTION WELDING OF NICKEL BASE SUPERALLOYS FOR AEROSPACE APPLICATIONS

G.J. Baxter¹, M. Preuss² and P.J. Withers²

¹ Manchester Materials Science Centre, UMIST/University of Manchester, Grosvenor St.,
Manchester M1 7HS, UK

² Rolls-Royce plc, Derby DE24 8BJ, UK

INTRODUCTION

A new generation of nickel-base superalloys having a significantly higher volume fraction of γ' than conventional superalloys has been developed in order to meet the demand for better high temperature properties. These alloys are typically very difficult to weld and are prone to micro-cracking as solidification takes place during welding [1, 2]. Therefore inertia friction welding is a very attractive joining process since it does not involve any melting, provided optimum welding parameters are chosen. Furthermore, it is more suitable for production than electron beam welding since it does not require a vacuum environment [3]. Inertia friction welding also enables one to weld dissimilar alloys, which can be difficult by other means. Rolls-Royce is employing inertia friction welding to join high pressure compressor drums, turbine discs and shafts on the recently installed 2000 ton force inertia welder near Nottingham, UK (Fig. 1).

During inertia friction welding, one of the work pieces is connected to a flywheel and the other is restrained from rotating. The flywheel is accelerated to a predetermined rotational speed then disengaged and the work pieces are forced together by applying axial pressure. This first stage of inertia friction welding ends when the nominal pressure has been achieved and can be characterized by an initial torque peak (Fig. 2). At this point, the parts have not lost any axial length (loss in length, $U = 0$). During the second or conditioning stage, kinetic

energy stored in the rotating flywheel is dissipated as heat through friction at the weld interface. This takes place over a short time span with a reasonably flat torque curve. This means that the material reaches forging temperature at the interface within 2 to 10 seconds, depending on the material and welding parameters. As a result of the axial pressure and the continued high energy input to the weld interface, material is squeezed out at the interface resulting in weld flash and loss in length from both parts (stage 3). In the final or forging stage the flywheel slows to zero speed and material in the weld interface region is lost in the flash. This stage is characterized by a second sharp torque peak, because the temperature of the material at the weld line has started to decrease. The pressure is maintained after all kinetic energy has been imparted to ensure a sound metallurgical joint. In order to generate joints with a correct loss in length and optimum metallurgy a detailed understanding of the inertia friction welding parameters is essential.

One alloy, which at the present time can only be welded by inertia friction welding is RR1000, a recently developed powder-processed, high strength nickel-based superalloy. It comprises a high volume fraction of primary γ' (1-3 μm), secondary γ' (50-500 nm) and tertiary γ' (5-30 nm). In the parent alloy, particles of γ' , which remain undissolved during the solution heat treatment stage (primary γ'), delineate γ -grain boundaries while intragranular γ' precipitates upon cooling with a bimodal distribution (secondary and tertiary γ'). Whereas particles of secondary γ' nucleate at an early stage during cooling from the solution temperature, tertiary γ' nucleates at a lower temperature, when diffusion rates are slow and secondary γ' cannot grow sufficiently quickly during cooling [4].

This paper presents results from investigations of residual stresses, metallurgy and mechanical properties of inertia friction welded RR1000 joints.

EXPERIMENTAL

Materials and Specimens

The chemical composition of RR1000 [5] is listed in Table 1 alongside those for UDIMET 720LI & Waspaloy [6] for comparison. This shows that RR1000 has a much larger wt% of Al and Ti than Waspaloy and consequently a significantly higher volume fraction of γ (γ is $(\text{Ni, Co})_3(\text{Al, Ti})$ [7]). This is expected to affect markedly the development of microstructure and residual stress during inertia friction welding. The RR1000 material used for this investigation came from an isothermal pancake forging, fully heat-treated and annealed. Rings were machined from the pancake and subsequently inertia welded at MTI, South Bend, Indiana, USA. All studies were carried out on three welds made with the same welding parameters. Weld 1 was examined in the as-welded condition and weld 2 was post weld heat treated (PWHT'd) using an conventional post weld heat treatment. After the initial round of residual stress measurements, weld 1 was given a modified PWHT that was 50°C above the established one. Weld 3 was sectioned to study the microstructure and mechanical properties of the three different conditions.

Neutron diffraction measurements

All measurements were carried out on the ENGIN diffractometer at the ISIS neutron spallation source, Rutherford Appleton Laboratory, UK. At pulsed neutron sources, neutrons of all wavelengths emerge over a short time pulse from the source. With detectors placed at a given angle the whole diffraction profile can be recorded as a function of time of flight (TOF) [8]. The sampling gauge volume is defined by the intersection of the incident and diffracted beams. The lattice parameter, a , of the lattice planes with plane normal bisecting the incident and diffracted beams, averaged over the correctly oriented grains within the sampling volume, was determined by Rietveld refinement of the spectra [9]. A more detailed description of the application of neutron diffraction for engineering strain scanning can be found elsewhere [10,

11]. The variation in the lattice spacing was mapped out over a cross-sectional plane at a specific hoop location for all three specimens over a region extending from the weld line up to 8 mm away from it. A previous experiment [12] had indicated that the residual stresses in a similar weld were essentially symmetric about the weld line ($z = 0$). Consequently, measurements were only made on one half of the coordinate system ($z > 0$). The sample coordinate system as defined for the experiment is shown in Fig. 3.

The strains were calculated at all points using:

$$\varepsilon(r, z) = \frac{a(r, z) - a_0(z)}{a_0(z)} \quad (1)$$

where a_0 is the stress-free lattice parameter.

It was shown in [13] that the stress-free lattice spacing varies only as a function of z . As a consequence, it can be determined by forcing the axial stresses to be balanced across the wall section. Note that for a tubular structure moment need not balance across a single tube wall. The corresponding axial, radial and hoop residual stress fields for the three welds were calculated using:

$$\sigma_{axial} = \frac{E}{(1 + \nu)(1 - 2\nu)} [(1 - \nu)\varepsilon_{axial} + \nu(\varepsilon_{radial} + \varepsilon_{hoop})], \text{ etc} \quad (2)$$

where E is the bulk Young's modulus, and ν the Poisson's ratio. Use of the bulk value of E was justified because the Rietveld refinement included 7 diffraction peaks. Even though all stress directions were calculated, this paper only presents the results of the hoop stress fields as they are of the largest magnitude and therefore of most interest.

Hole drilling

Without compensation, neutron diffraction strain measurements made very near to the surface are vulnerable to serious errors, when the gauge volume is not fully immersed in the bulk

material [14]. The recorded diffraction peak is a statistical distribution of the contributions from all the diffracting crystals in the gauge volume. When the gauge volume is only half immersed in the material, the statistical distribution of the diffraction peak is changed and results in a so-called geometrical pseudostrain [15]. Therefore, hole-drilling is a more appropriate technique for near surface residual stress measurements. Residual stresses have been determined from strain measurements using the target strain gauge / center hole drilling method to a maximum depth of 0.64 mm from the surface (gauge length: 0.79 mm, drill diameter: 0.9 mm). Three sets of gauges have been installed in 120° angular locations to each other at the inner and outer surface of the weld line. The integral method, which is based on a linear elastic model, was used to calculate the hoop and axial residual stresses from the strain changes during hole-drilling [16].

Hardness testing

Hardness testing was carried out under a load of 1kg using a calibrated Vickers hardness indentation machine. For each sample, measurements were carried out on a weld cross section on a grid of 5 lines parallel to the axial direction and spaced greater than 4 indentations apart. Measurements were taken from the weld line to a distance 9 mm away from it, with smaller increments close to the weld line. The accuracy of the axial position of the indentation marks was estimated to be within 20 µm. The results presented are the average of the 5 measurements per axial position.

Spatially resolved strain measurements during tensile straining

Locally resolved strain measurements were carried out during tensile testing using the electronic speckle pattern interferometry (ESPI) technique. ESPI is a technique that exploits the properties of expanded lasers when they are directed at an optically rough surface [17]. When a defocused laser is directed at a diffusely reflecting surface it is scattered in many directions. These reflected wavelets then interfere constructively or destructively, depending

on the observation plane. Interference with an additional reference laser renders the speckle pattern sensitive to in-plane displacements. The interference between the live and the previous image (reference image) results in a pattern of correlation fringes, when the reference image is subtracted from the live image. The spacing of these fringes is related to the sample displacement. This effect only occurs if coherency is maintained. As a result, large displacements must be recorded by combining the data from many consecutive laser speckle measurements. For this experiment, tensile testing was carried out on an Instron tensile rig equipped with a 50kN load cell and a commercial '3D' ESPI system, produced by Ettemeyer, Germany. The displacement rate of the head section was 0.01 mm/s, which corresponds to an initial strain rate of 5×10^{-4} 1/s with tensile samples having a gauge length of 20 mm. The tensile samples were cut such that the weld line was normal to the tensile axis with the weld carefully positioned along the gauge length. During loading, speckle pattern images were taken every 1.7 seconds resulting in a sufficient number of speckle patterns to accurately describe the elastic and plastic deformation of the tensile sample as a function of applied stress. The consecutive speckle patterns were analyzed to produce a series of two dimensional displacement maps. Since the strain was independent of R , the strains were averaged at each z value over all R . Given that the strain varies only as a function of z , which is also the tensile axis, it is fair to assume the stress is the same everywhere. On this basis, it was possible to infer the stress-strain response as a function of z with a spatial resolution of 30 μm . These stress/strain curves were then used to determine the 0.2 % yield stress as a function of axial position.

Synchrotron X-ray measurements:

Diffraction profile measurements can be used to assess the fraction of γ' across the welded region on the basis of the intensity of the superlattice reflections. To this end, high resolution synchrotron X-ray diffraction profile measurements were carried out on the ID11 beam line at

the European Synchrotron Radiation Facility (ESRF) in Grenoble, France using a scanned serial detector. The high intensity of the synchrotron beam allowed accurate measurements of the (100) superlattice reflection, arising from the ordered γ' phase (LI_2 structure). Since the (100) reflection is systematically absent for the disordered γ matrix phase, by normalizing the integrated intensity of the superlattice reflection with the integrated intensity of the (200) reflection, any influence of texture variations on the measurement could be eliminated and the obtained value related to the volume fraction of γ' [18, 19, 20]. Because large peak broadening of the (200) reflection was observed around 1 mm from the weld line, the (200) reflection of the as-welded sample was studied across the weld line in a second synchrotron experiment on ID31, ESRF, Grenoble. By scanning the (200) reflection with a high level of accuracy, it was possible to deconvolute the (200) γ and (200) γ' reflection in the region close to the weld line. The strain (coherency strain) between the two phases was then calculated using equation 2.

Electron microscopy and image analysis

The particle size and volume fraction of γ' as a function of axial position were studied by using a Philips XL30 FEGSEM in the secondary electron mode at 8 kV at a working distance of 10 mm. The high resolutions of the FEGSEM allowed the analysis of primary, secondary, and in the case of the modified post weld heat-treated samples, tertiary γ' . Image analysis of secondary and tertiary γ' was carried out using the Kontron KS 400 software package. Five images at each axial position were taken within γ grains, avoiding primary γ' . Consequently the determined volume fractions of secondary and tertiary γ' should be regarded as values in the centre of γ grains and not a true overall value.

Automated electron backscatter diffraction mapping was employed to study γ grain size variations across the weld line. During EBSD mapping the beam was scanned over the

polished sample, which was tilted 70° to the backscatter detector of a Philips XL30 FEGSEM. EBSD patterns were detected by a CCD camera with the background subtracted using an image processor. Seven area maps were acquired across the weld line using a scanning step size between 0.27 and 0.35 μm. The EBSD data were analyzed using VMAP, an in-house software development by F.J. Humphreys *et al.* [21] and the Channel software package [22].

RESULTS AND DISCUSSION

Residual stresses

Fig. 4 shows the results of the neutron diffraction measurements for the hoop stress fields for a) as-welded, b) conventional and c) modified post weld heat treated conditions. The contour maps were calculated from 20 measurement positions with an average stress uncertainty of 60MPa. The maximum hoop residual stress in the as-welded specimen is in the range of 1500 MPa at the weld line close to the inner diameter (R=-4). Note that at the outer diameter, residual stresses do not exceed 700 MPa. After exposing the joint to the established post weld heat treatment for nickel-base superalloys, the stress magnitude in weld 2 was reduced by about 30%. The maximum stress in the hoop direction is around 1000 MPa. A stress gradient at the weld line between the positions close to the inner and outer diameter is still apparent. The hoop stresses of weld 2 show that the conventional PWHT is not completely effective. After increasing the PWHT temperature by 50°C (modified PWHT), the maximum stress in the hoop direction is now less than 400 MPa and the stress difference between the inner and outer surface region has vanished.

The hole drilling results confirm the large residual stresses in the as-welded (weld 1) and conventional post weld heat treated (weld 2) specimens and the relatively low stresses in the modified post weld heat treated specimen (Fig. 5). In the as-welded specimen, large tensile stresses are observed for the axial and hoop direction about 0.3 mm beneath the surface (Fig.

5a). However, when residual stresses approach the material yield stress, hole drilling results have to be treated with caution. For this reason the measurements near the inner diameter in the as-welded condition are unreliable. Since the residual stresses close to the outer diameter do not approach the yield point of the material, the hole drilling results from the outer diameter are more reliable and in good agreement with the neutron diffraction results. It can be seen in Fig. 5a that the axial stresses are tensile close to the inner diameter changing into compression close to the outer diameter, which indicates a bending moment in the weld [12]. The post weld heat treated samples (weld 2 and 3) show excellent agreement between the hole drilling and neutron diffraction results (Fig. 5 b,c) and confirm the need to increase the PWHT temperature by 50°C in order to reduce the residual stresses sufficiently.

Mechanical properties

Steep gradients in the hardness are observed for the as-welded condition (Fig. 6). A trough in hardness occurring approximately 1 mm from the join line is bounded by two peaks situated at 0.3 mm and 2 mm from the weld line. After conventional post weld heat treatment an increase in hardness in the weld region is observed such that the peak at 2 mm is subsumed within the upward curve towards the weld line and the trough is replaced by a discontinuity in slope. Near the weld line the hardness is about 50 H_V higher than in the parent material. An increase of 50°C to the conventional PWHT temperature does not result in any major changes of the hardness profile or peak hardness value. However, the discontinuity observed at 1 mm in the conventionally PWHT'd sample has disappeared. Fig. 7 shows the difference between the measured and the nominal 0.2 % yield stress distribution (measured – nominal 0.2 % yield stress) of RR1000 across the weld line for the conventional and modified PWHT'd conditions. The 0.2 % yield stress profiles exhibit great similarities with the hardness profiles presented in Fig. 6. At any axial position, both conditions display a 0.2 % yield stress well above the nominal value of this alloy: (at least 25 MPa above the requirement). Some scatter

of the yield stress in the parent material can be seen with the conventionally post weld heat treated sample exhibiting a difference of about 40 MPa for the two sides from the weld line ($z = \pm 6$ mm). This range of scatter is however quite typical for such materials. Fig. 7 shows that the overall yield stress distribution of the modified post weld heat treated sample (50°C above the conventional PWHT) is on average only 20 MPa below the conventionally post weld heat treated sample. For both PWHT conditions, the 0.2 % yield stress at the weld line has improved by about 100 – 120 MPa compared to the parent material. Therefore in the region of the highest residual tensile stresses, the component benefits from a stronger microstructure. In the following section, emphasis is placed on analyzing the variation of the microstructure across the weld line to rationalize the hardness and 0.2 % yield stress profiles in the as-welded and post weld heat treated conditions.

Microstructure

γ' changes across the weld line

The (100) superlattice synchrotron X-ray reflection data in Fig. 8 shows that the as-welded sample is depleted of γ' until at least 2 mm away from the weld line. It is notable that the hardness drop (Fig. 6) and the maximum depletion of γ' occur at approximately the same axial position. This suggests that a significantly lower content of γ' is probably responsible for the hardness drop observed in the hardness profile for the as-welded sample. The conventional heat-treated sample also shows a zone impoverished of γ' within 2 mm of the weld line, although the drop of the normalized integrated intensity is less pronounced than in the as-welded condition. The drop in γ' could be responsible for the hardness discontinuity (see A in Fig. 6) at 1 mm. Virtually no alteration in γ' volume fraction was observed for the modified PWHT'd sample across the weld line suggesting that this treatment is sufficient to homogenize the γ' volume fraction (though not necessarily its distribution between primary, secondary and tertiary phases).

Fig. 9a and b are low magnification FEGSEM images of the γ' distribution for the as-welded condition at a) the weld line and b) 2.5 mm from the weld line. These two images demonstrate the dramatic variation of γ' distribution in the vicinity of the weld line. It was shown for the as-welded and PWHT'd samples in [23] that at the weld line, the volume fraction of primary γ' drops to zero, whereas beyond 1 mm from the weld line the primary γ' content is essentially constant at approximately 15%.

Fig. 10a-d are high magnification FEGSEM images of the modified PWHT'd sample showing the distribution of secondary and tertiary γ' at various distances from the weld line. At the weld line, all secondary γ' is in solution and only tertiary γ' was detectable (Fig. 10a). This feature was observed in the as-welded and both post weld heat-treated conditions. Significant changes in the secondary and tertiary γ' distribution can be observed over the first 2 mm from the weld line (Fig. 10a-c), whereas beyond 2 mm no significant changes in γ' are detectable (Fig. 10d). Fig. 11 compares the hardness profile with the variation in secondary and tertiary γ' content across the weld line for the modified PWHT'd sample. It can be seen that the change in volume fraction of tertiary γ' correlates well with the hardness peak close to the weld line. The importance of tertiary γ' in respect of mechanical properties has also been reported by Torster *et al.* [24], where it was observed that an increased volume fraction of tertiary γ' resulted in a higher proof stress. In general it is well accepted that an increase of the cooling rate from the solution temperature increases the tertiary γ' volume fraction and thus tensile strength [25].

Fig. 12 plots the coherency strain between γ and γ' for the matrix (γ) as a function of axial position measured from the (200) reflections on beam line ID31 at the ESRF. A dramatic change of coherency strain was recorded between the weld line and 4 mm from the weld line starting with essentially zero strain at the weld line, going through a maximum of about 4000

microstrain (0.4% strain) between 1 and 2 mm from the weld line, before it dropped back to zero at about 4 mm from the weld line. The variation of coherency strain can be explained in terms of γ' exposed to different temperatures during welding. Because cooling rates are severe after the heat input during joining is completed, it can be expected that the chemical composition of γ' is frozen at its maximum temperature during welding. Assuming that the chemical composition of γ and γ' at high temperatures results in high coherency strain at room temperature, one would expect the highest coherency strain at the weld line tailing off to zero within the HAZ. This can be partly seen in Fig. 12 with a declining coherency strain between 2 and 4 mm from the weld line. Between 2 mm from the weld line and the weld line, an increasing volume fraction of γ' gets dissolved during welding with all γ' dissolved at the weld line. As it was shown in [23], very fine reprecipitated γ' was found at the weld line, indicating that the driving force for precipitation of the alloying elements in RR1000 is large enough to partly reprecipitate γ' even under severe cooling rates. The post-weld formed γ' however must have precipitated at a fairly low temperature due to undercooling effects. Therefore the chemical composition of post-weld γ' can be expected to vary significantly from γ' , which was exposed to high temperatures during welding. Hence, the maximum coherency strain is not found at the weld line but between 1 and 2 mm from it. The essentially zero coherency strain at the weld line could be one factor for the slight drop of hardness towards the weld line as observed in Fig. 6. The increase of micro hardness (Fig. 6) and 0.2% yield stress (Fig. 7) starting at 4 mm from the weld line can be explained by the raise in coherency strain between γ and γ' .

High angle grain boundaries

Representative Euler maps for the as welded sample are shown in Fig. 13a-e. Due to the similar chemical composition and structure of γ and γ' , the maps can not distinguish between γ grains and primary γ' particles. The maps show a dramatic change in microstructure between

the weld line and 1 mm from the weld line. Beyond 1 mm from the weld line no discernable change in microstructure was observed. At the weld line (Fig. 13a) the high temperature reached has resulted in a fully recrystallized microstructure with a mean grain size (D) of 4.2 μm and an even grain size distribution. The sharp drop in D between the weld line and 0.25 mm is partly due to the fact that at the weld line D is only determined by γ whereas at 0.25 mm the mean grain size is a combination of γ and γ' . 0.5 mm away from the weld line (Fig. 13c) the microstructure exhibits large areas with very small grains where the microstructure has started to recrystallize under a combination of heavy plastic deformation and high temperature. In addition, large grains are visible, which have not yet started to recrystallize. The variation in grain size is presented as $D^{-0.5}$ across the weld line in Fig. 14. In a narrow region around 0.5 mm away from the weld line the grain size is reduced by almost 50%. Correlating Fig. 14 with Fig. 6 would suggest that the grain size does have an impact on the hardness peak very close to the weld line. It is noteworthy that, in the parent material (greater than 5 mm from the weld line) 27% of the HAGB were identified as twin boundaries, whereas at the weld line only 3.5% of the HAGB are twins. This is a consequence of recrystallization at the weld line. In [23] these EBSD maps were also analyzed in terms of misorientation between EBSD measurement points within one grain, which could be used to calculate the stored energy. It was found that at 0.5 mm from the weld line, in the region where recrystallization starts to occur, the stored energy displayed a sharp maximum.

SUMMARY AND CONCLUSIONS

This paper demonstrates the importance of managing the microstructural aspects and mechanical properties together with residual stress issues in inertia friction welded nickel-base Superalloys. It was found that for inertia friction welded RR1000 large tensile hoop stresses can be detected after welding. Only after increasing the temperature by 50°C above the conventional PWHT were the hoop stresses relieved to an acceptable level (below 400

MPa). Results of neutron diffraction strain mapping experiments were supported by depth profiling measurements made by hole drilling carried out at the inner and outer diameter of the weld line. The results however also demonstrate the limitation of hole drilling, when the residual stresses are close to the yield point. The recording of micro hardness and 0.2 % yield stress profiles, using an electronic speckle pattern interferometry technique showed that both post weld heat treated conditions have similar strength distributions across the weld line. No significant loss of 0.2 % yield stress could be observed after increasing the PWHT temperature by 50°C, which suggest that this modified PWHT is appropriate for inertia friction welded RR1000. In the region of largest residual tensile stresses, at the weld line, the 0.2 % yield stress of RR1000 was about 100-120 MPa higher than in the parent material. The microstructure has been studied by means of high-energy synchrotron X-rays, electron microscopy and EBSD. No single microstructural parameter determines the complete response. Instead, the variations in tertiary γ' , coherency strain between γ and γ' , grain boundary strengthening and work hardening are the most important microstructural features determining the hardness profiles across the joint line.

ACKNOWLEDGEMENTS

The authors would like to thank Dr. A. Terry and Dr. G. Vaughan (ID11) and Dr. François Fauth (ID31) for their experimental support at the ESRF. Synchrotron beam time was made available through a long term development project (**me103**, P. Webster, P.J. Withers and A. Kosansky) for using synchrotron radiation for engineering strain scanning. We would also like to thank Dr. M.R. Daymond (ISIS, ENGIN) and Ian Brough (MMSC) for experimental assistance and Colin Small, Peter Wilson and Kevin Bass (Rolls-Royce plc.) for advice. These experiments are performed under the EPSRC project GR/M68704 and are financially

supported by EPSRC and Rolls-Royce plc. P.J. Withers acknowledges a Royal Society Wolfson Research Merit Award.

Captions:

Table 1: Chemical composition (wt%, balance nickel) of RR1000 and other disc alloys.

<i>Alloy</i>	<i>Cr</i>	<i>Co</i>	<i>Mo</i>	<i>W</i>	<i>Al</i>	<i>Ti</i>	<i>Ta</i>	<i>Hf</i>	<i>Zr</i>	<i>C</i>	<i>B</i>	$\gamma_{vol\%}$
RR1000	14.35- 15.15	14.0- 19.0	4.25- 5.25	-	2.85- 3.15	3.45- 4.15	1.35- 2.15	0.0- 1.0	0.05- 0.07	0.012- 0.033	0.01- 0.025	48
U720LI	16	15	3.0	1.25	2.5	5.0	-	-	0.035	0.015	0.015	45
Waspaloy	19.5	13.5	4.3	-	1.3	3.0	-	-	-	0.08	0.006	25



Fig. 1: 2000 ton-force inertia welding machine installed at Rolls-Royce plc near Nottingham, UK.

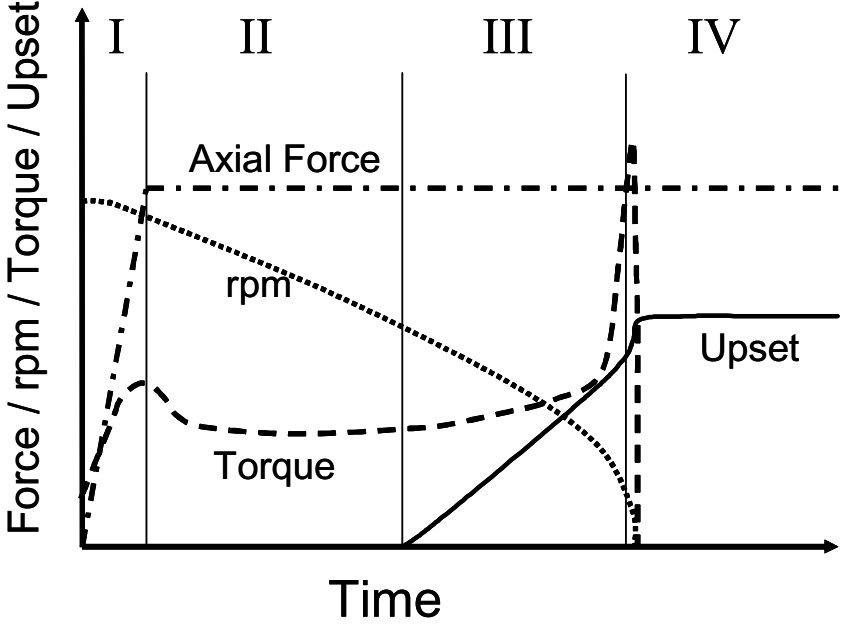


Fig. 2: Schematic graph of the four different stages during inertia friction welding

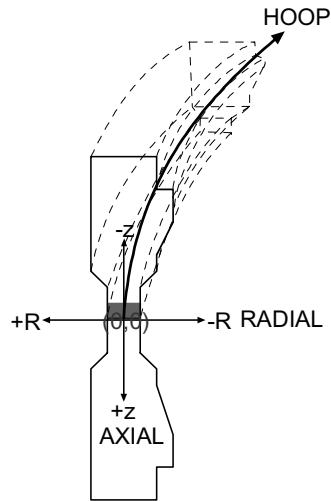


Fig. 3: The coordinate system of the measured cross section. The shaded region highlights the areas where the measurements were made.

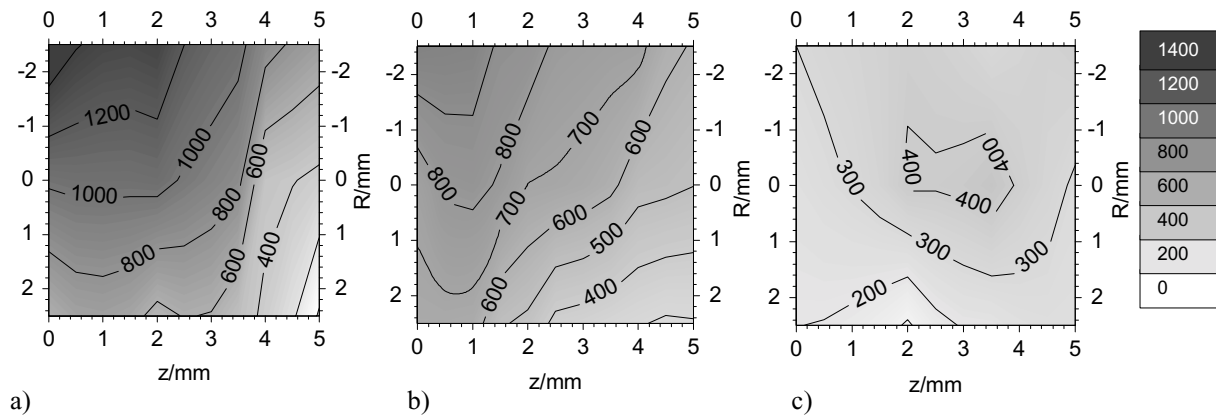


Fig. 4: Contour plots of the hoop stresses in RR1000 for the a) as-welded, b) conventional PWHT and c) modified PWHT condition.

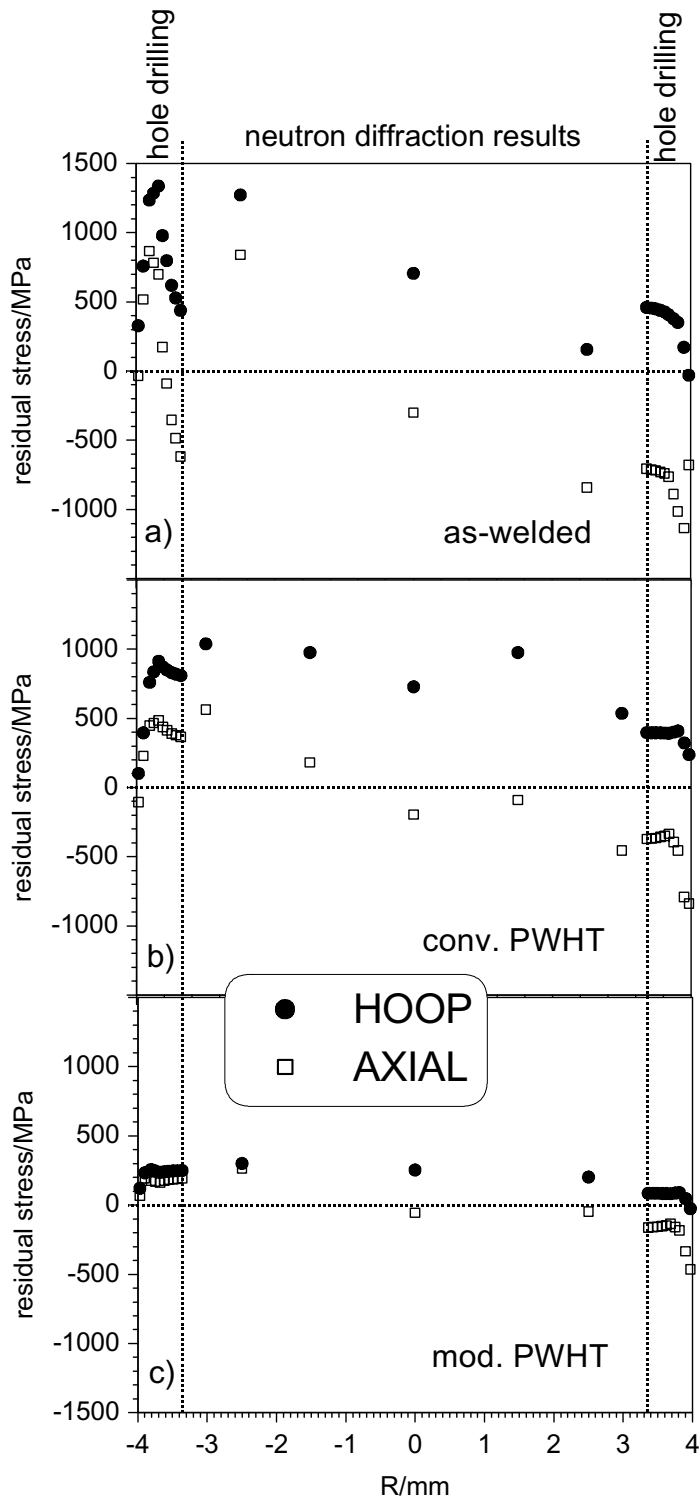


Fig. 5: Hole drilling and neutron diffraction results from the weld line for the axial and hoop stresses as a function of radial position. Results are plotted for the as-welded (top), conventional PWHT (middle) and modified PWHT (bottom).

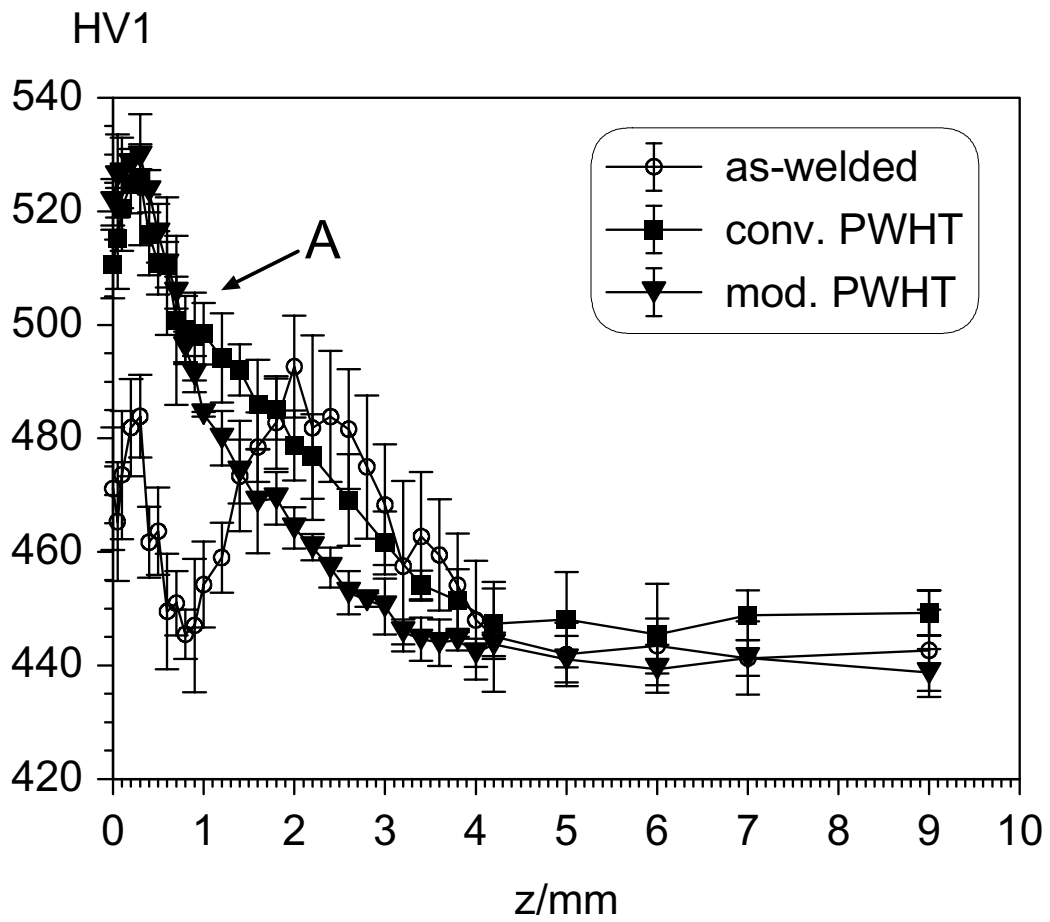


Fig. 6: Vickers hardness profiles of the as-welded, conventional PWHT'd and modified PWHT'd RR1000 samples as a function of axial distance from the weld line ($z=0$) measured at the mid-wall thickness.

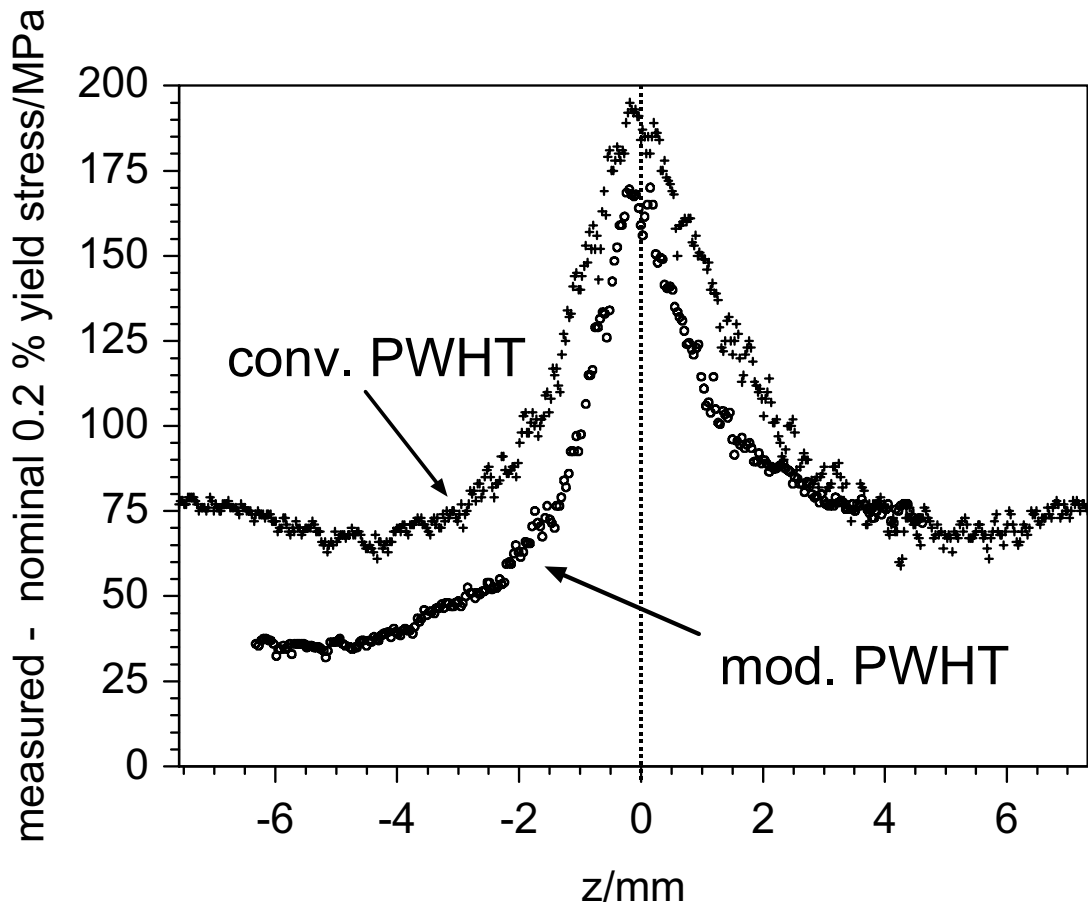


Fig. 7: 0.2 % yield stress profiles (measured – nominal 0.2 % yield stress) of the conventional and modified PWHT'd RR1000 samples as a function of axial distance from the weld line ($z=0$). The tensile tests were performed with an initial strain rate of 5×10^{-4} 1/s .

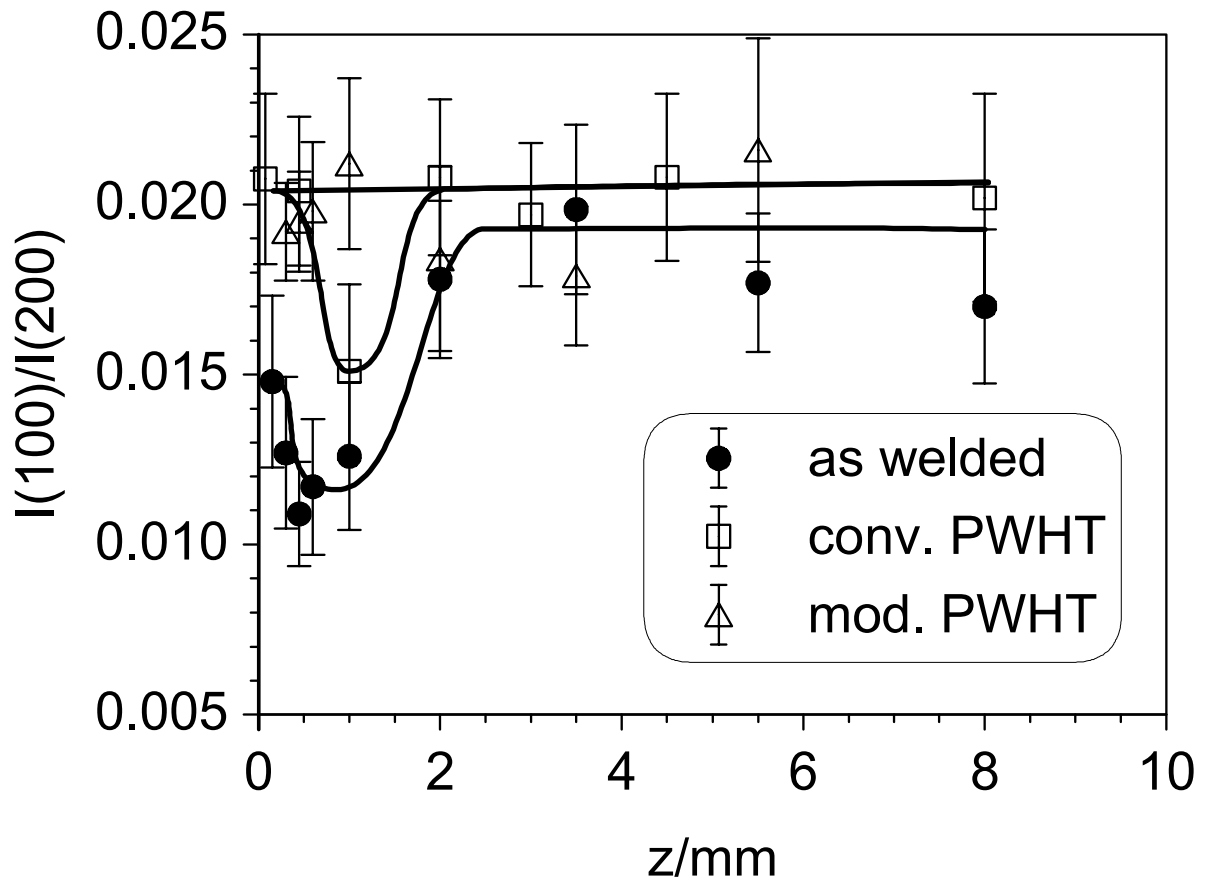


Fig. 8: The normalized ($I(100)/I(200)$) integrated intensity of the γ' superlattice reflection measured on ID11 at the ESRF plotted against the axial distance from the weld line.

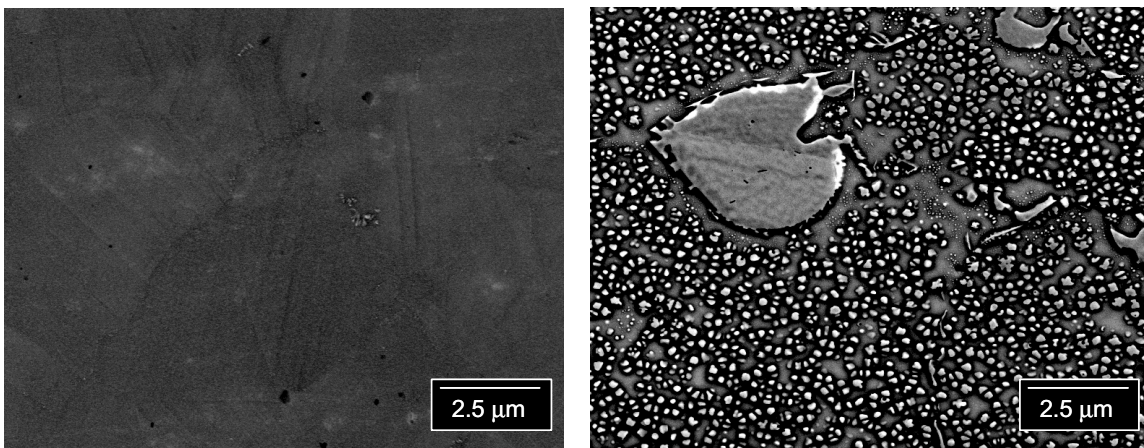


Fig. 9: Representative low magnification FEGSEM images of γ' in the as-welded condition a) at the weld line, b) 2.5 mm from the weld line.

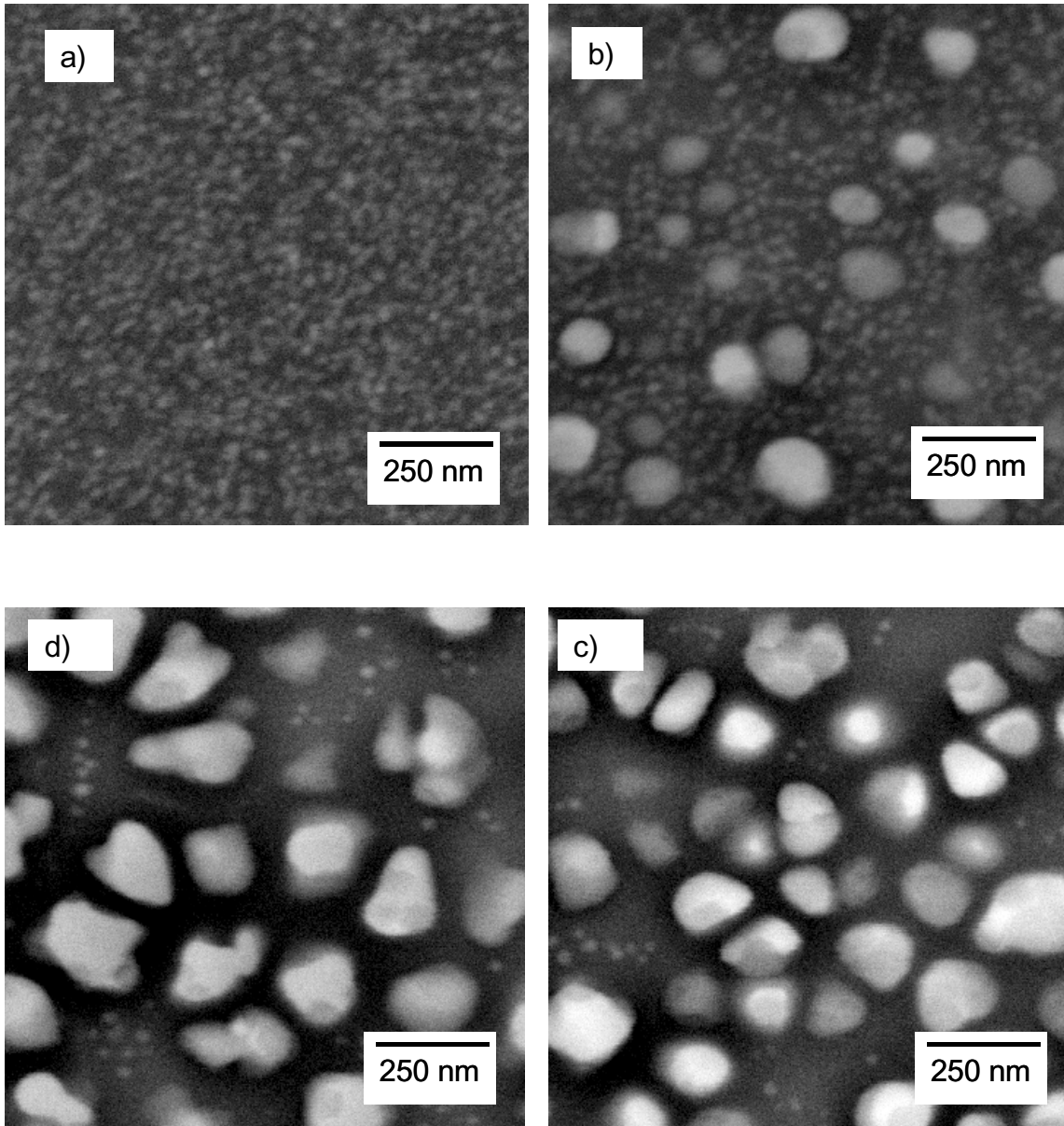


Fig. 10: Representative high magnification FEGSEM images of secondary and tertiary γ' of the modified PWHT'd sample a) at the weld line, b) 0.5 mm, c) 2 mm and d) 9 mm from the weld line.

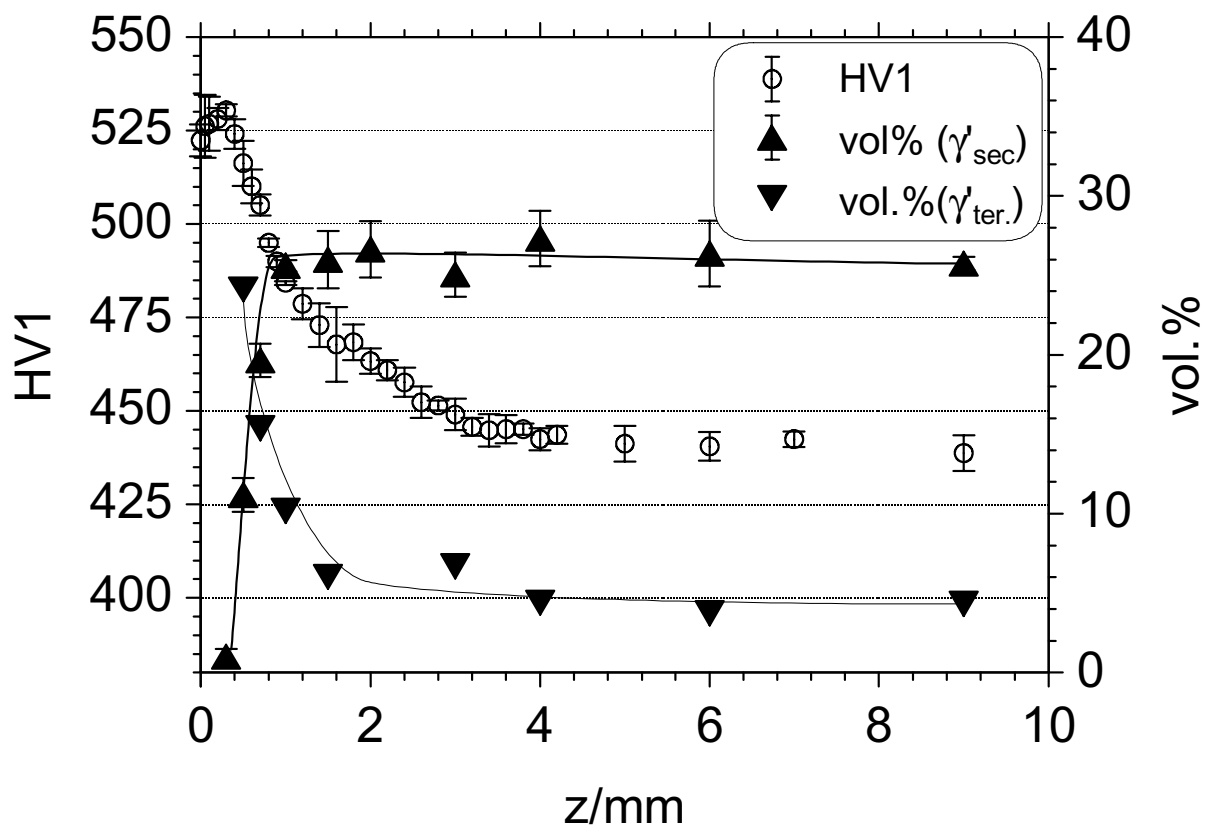


Fig. 11: Comparison between the micro hardness profile and the secondary and tertiary γ' distributions across the weld line for the modified PWHT'd sample.

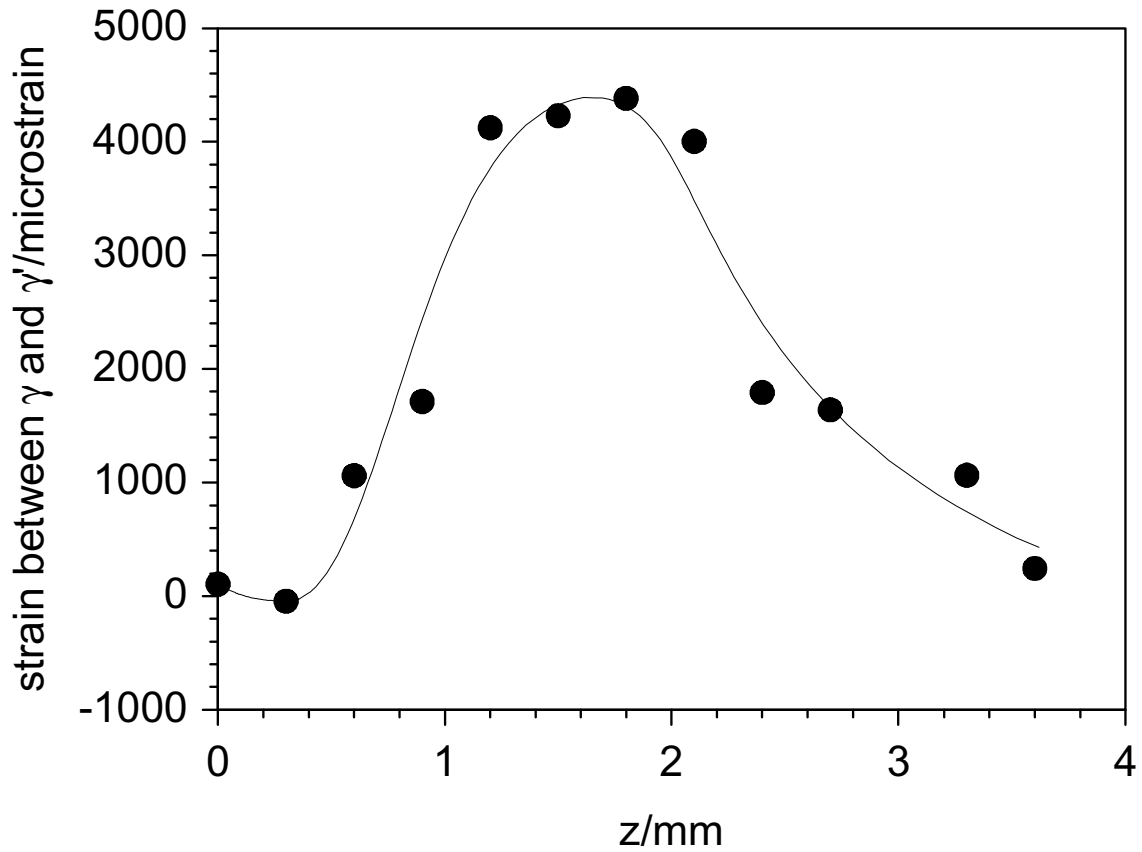


Fig. 12: Coherency strain between the γ matrix and γ' for the matrix measured on the as-welded sample from the (200) reflection on beam line ID31, ESRF.

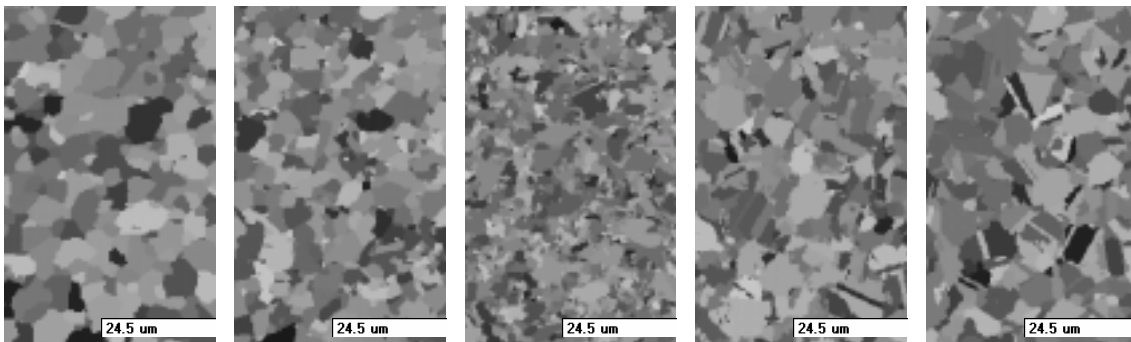


Fig. 13: Euler maps recorded by EBSD showing the γ grain and primary γ' distribution of the as-welded sample a) at the weld line, and b) 0.25 mm, c) 0.5 mm, d) 1 mm and e) 5 mm away from it. These views are representative of larger maps containing >1500 grains for which the average % twin boundaries were 3.5, 5, 11, 18 and 27.

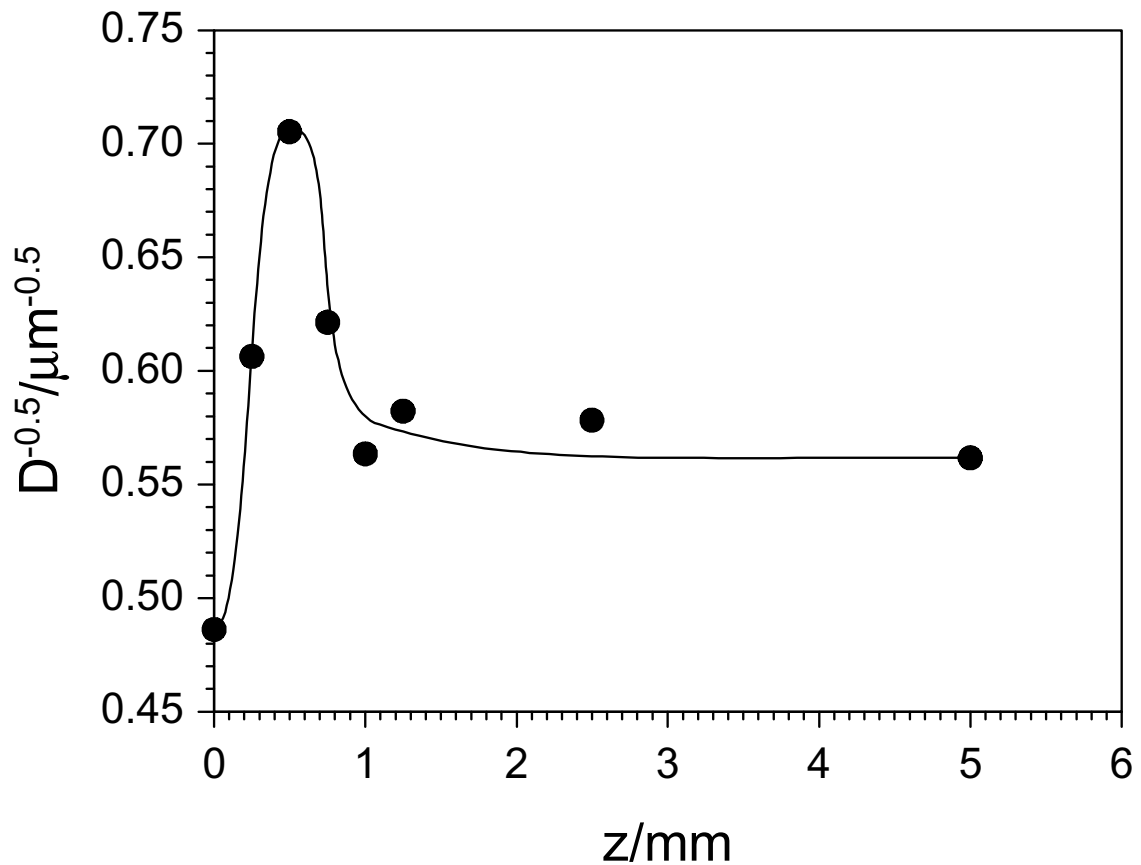


Fig. 14: The grain size in form of $D^{-0.5}$ across the weld line for the as-welded sample as recorded by EBSD mapping.

[1]: J.K. Tien and T. Caulfield (eds): Superalloys, Supercomposites and Superceramics, Academic Press INC (London) LTD, 1989, pp. 142-143.

[2]: C.T. Sims and W.C. Hagel (eds.): The Superalloys, John Wiley, New York, 1972, pp. 509-532.

[3]: R. Spinat and Y. Honnorat: High temperature alloys for gas turbines and other applications, W. Betz et al. eds., Dordrecht D. Reidel (1986), pp. 151-157.

[4]: M.P. Jackson and R.C. Reed: Mater. Sci. Eng. A, vol. 259, 1999, pp. 85-97.

[5]: S.J. Hessel et al., Nickel Alloy for turbine engine components, United States Patent Number 5897718 (27 April 1999).

-
- [6]: C.T. Sims, N.S. Stoloff and W.C. Hagel (eds.): Superalloys II, High Temperature Materials for Aerospace & Industrial Power, New York, NY: John Wiley & Sons inc., 1987, pp. 221-226.
- [7]: C.T. Sims and W.C. Hagel (eds.), The Superalloys, John Wiley, New York, 1972, pp. 44.
- [8] : M. W. Johnson, L. Edwards, and P. J. Withers: Physica B, vol. 234, pp. 1141-1143, 1997
- [9]:R.A.Young: Rietveld method, Oxford University press (Oxford), 1993.
- [10] : M. W. Johnson, L. Edwards, and P. J. Withers: Physica B, vol. 234, pp. 1141-1143, 1997
- [11]: I.C. Noyan and J. B. Cohen, Residual Stress, Springer Verlag, NYC, 1987, 111-116.
- [12]:J.W.L. Pang, M. Preuss, P.J. Withers, G.J. Baxter and C. Small, accepted for publication in Mat. Sci. Eng. A Nov. 2001.
- [13]: M. Preuss, J.W.L. Pang, P.J. Withers and G.J. Baxter: Metallurgical and Materials Transactions A, Volume 33A, Oct. 2002, 3127-3234.
- [14]: P.J. Webster, G. Mills, X.D Wang, W.P. Kang, T.M. Holden, J. Neutron Res. 3 (1996) 223-240.
- [15]: D. Wang, I.B. Harris, P.J. Withers, L. Edwards: in S. Denis et al., ECRS4, S. Denis, J.-L. Lebrun, B. Bourniquel, M. Marral, J.-F. Flavenot (Eds.), Cluny en Bourgogne, France, 1996, pp. 69-78.
- [16]: Determining Residual Stresses by the Hole-Drilling Strain-Gauge Method, ASTM Standard E837, ASTM, Philadelphia, USA, 1989.
- [17]: P.K. Rastogi, Principles of holographic interferometry and speckle metrology, in: Photomechanics, P.K. Rastogi (Ed.), Springer-Verlag, Heidelberg, 1999, pp. 103-145.
- [18]: A. Royer, P. Bastie and M. Véron: Scr. Mater., Vol 37, pp. 1199-1205.
- [19]:A. Royer, P. Bastie and M. Véron: Scr. Mater., Vol 40, pp. 955-961.
- [20]: A. Royer, P. Bastie and M. Véron: Acta Mater., vol. 46, 1998, pp. 5357-5368.

[21]: Software and user manual at:

<http://www.umist.ac.uk/material/research/aluminum/frame.html>.

[22] Channel 4.2: HKL Technology ApS, Blaakildevej 17k, Hobro, DK-9500, Denmark.

[23]: M. Preuss, J.W.L. Pang, P.J. Withers and G.J. Baxter, Metallurgical and Materials Transactions A, Volume 33A, Oct. 2002, 3115-3225.

[24]: F. Torster, G. Baumeister, J. Albrecht, G. Luetjering, D. Helm and M.A. Daeubler: Mater. Sci. Eng. A, vol. A234, 1997, pp. 189-192.

[25]: J.J. Schirra and S.H. Goetschius: Superalloys 1992, S.D. Antolovich, R.W. Stusrud, R.A. Mackay, D.L. Anton, T. Khan, R.D. Kissinger, D.L. Klarstrom (eds.): The Mineral, Metals & Materials Society, 1992, pp. 437 – 446.